Resonant Waveguide vs Fabry-Perot Cavity: A Comparative Study for CMOS Spectral Sensor Technology

Fatima Omeis, Sandrine Villenave, Mondher Besbes, Christophe Sauvan, H. Benisty

Resonant Waveguide vs Fabry-Perot Cavity: A Comparative Study for CMOS Spectral Sensor Technology

Fatima Omeis[a], Sandrine Villenave[a,b,c], Mondher Besbes[a], Christophe Sauvan[a], Henri Benisty[a,*]

[a]*Université Paris-Saclay, Institut d'Optique Graduate School, CNRS, Laboratoire Charles Fabry, Palaiseau, France*
[b]*STMicroelectronics, 38920 Crolles, France*
[c]*Université Grenoble Alpes, CEA Leti, Grenoble, France*

Abstract

The ubiquitous use of versatile smart devices fuels a rapid growth in spectral sensor technology. Ambient Light Sensors (ALS), with 3–6 spectral channels in the visible and near-infrared are the most common version today. Their architecture comprises a pixel and a filter atop. While the compliance of the pixel to CMOS technology is built-in, the compliance of the filter in terms of materials and of process parallelism is not obvious. The process demand discards the pixel-scale variable-thickness Fabry-Perot solution, notably, and rather points to single-step nanophotonic structures whose pattern is specific to each ALS pixel/channel. In this study, we provide a performance comparison between two such candidate filters, the resonant waveguide (RWG) rejection filter, and the hybrid Fabry Perot (FP) band-pass filter. The evaluation is carried out in terms of spectral response, tunability, angular and polarization tolerance, and noise sensitivity, assessing the collective ability of an ALS array to retrieve spectral information. Through this analysis from the photon to the system, we pave a methodological frame for engineers and manufacturers facing a variety of application choices and sensing capabilities.

Keywords: grating filter, CMOS compatible, Ambient Light Sensor, Angular tolerance, spectral retrieval
PACS: 42.79.Dj, 85.60.Gz, 07.57.Ty

---

*corresponding author

1. Introduction

Thanks to miniaturization, driving the ubiquitous use of smartphones and associated cameras in all environments, there is a rapidly growing demand for integrated spectral sensors with various functions [1, 2, 3, 4, 5]. Among these, ambient light sensors (ALS), especially for operation in the far red + near-infrared ranges, are of interest in smartphone cameras, color correction, screen-brightness adjustment and intended surveillance and monitoring systems [6, 7, 8, 9, 10, 11, 12, 13]. The embedded filters that come atop each large pixel of an ALS could be made by variable thickness Fabry-Perot, but this choice incurs too costly multiple deposition+masking processes for more than 3–5 channels in the CMOS context that is unavoidable to get low-cost mass production [14, 15, 16]. A more rational choice within this demand rests on the interaction of light with subwavelength structures (dielectric or metallic) [17, 18, 19, 20].

Many general studies showed that nanostructured plasmonic surfaces, which are typically based on the use of patterned thin metallic films (i.e., Au, Ag, or Al), compliant with a single or a few deposition steps, can achieve a large tunability and a large angular tolerance over the visible spectral range[20, 18, 21], thanks to their inherently strong light-matter interaction. But the downside of such plasmonic filters is that their efficiency is relatively low due to the significant optical losses of metals, and their fabrication process is not fully compatible with CMOS technology, making them a weak competitor for the current industrial challenges. On the other hand, subwavelength gratings made in silicon-based dielectric materials have lower intrinsic losses, especially in the targeted near-infrared range, yielding color filters with higher luminosity [22]. This makes dielectric structures more suitable to improve the spectral features of CMOS image sensor devices in terms of resonant behavior and tunability [23, 24].

By varying the lithographically accessible geometry of the dielectric nanostructures, the position of the resonances can be tuned throughout the visible and infrared range [25]. Many studies were carried out to understand and fabricate dielectric and metal-based spectral filters possibly with angular insensitive properties [26, 27] but rather with a focus on highly efficient reflection when using either simple resonant waveguide grating structures whose function is similar to well-known periodic stacks commonly named as

Distributed Bragg Reflectors (DBRs).

There are many context-dependent challenging aspects for these filter technologies [28] such as being ultraviolet-robust, performing better or new photonic functions such as narrow-band and/or highly angular tolerant filtering to combine filtering with efficient light collection in large apertures and improve signal-to-noise ratios. In this study we adopt a particular case of ALS sensor and exploit the bare filtering results in ways that make sense one level higher, in terms of a system for spectral retrieval of elementary spectral features.

We will specifically provide a guide for ALS filter choice by exploring, comparing, and evaluating the performance of two potential designs for spectral filters in red to near-infrared ranges, the resonant waveguide grating (RWG) and the hybrid Fabry-Perot (h-FP) cavity designs [29], this latter comprising a periodic in-plane structure inside the cavity. The spectral response of both structures will be studied and compared, while their tunability is tested, taking into account parsimony in the fabrication process steps, limited here to a single value for the pattern period. The dispersion provided by nanostructures is further exploited to enhance the angular tolerance, with the outcome for both TE and TM polarizations being discussed. Going to the ALS array level, a comparative study on the signal-to-noise performance in terms of coarse spectral retrieval is reported for both types of configurations. It is based on the useful case of chlorophyll (green plant leaves) diffuse reflection, low in the red but high in the near-infrared.

Finally, light collection in both structures is investigated for a large range of incident angles.

2. Structures design, spectral response, and tunability

We shall use the conventions of Fig.1 to address TE and TM incident waves of variable angles of incidence and azimuthal angles, with in-plane wavevector $\mathbf{k}_\parallel$. We will refer to normal incidence according to $\varphi = 0°\ (= \theta)$ of this figure as well, thus setting Cartesian field components in this limit case as E_y and H_x.

The RWG filter is represented schematically in Fig.2(a), it consists of a thin layer ($h_g = 25\,\text{nm}$) of refractive index $n_{Si} = 4.0$, which is an approximation of that of amorphous Si (a-Si) in the spectral range studied, and a square a-Si grating of thickness $h_r = 50\,\text{nm}$. On the other hand, the h-FP filter, shown in Fig.2(b), is composed of a square grating of thickness $h_f =$
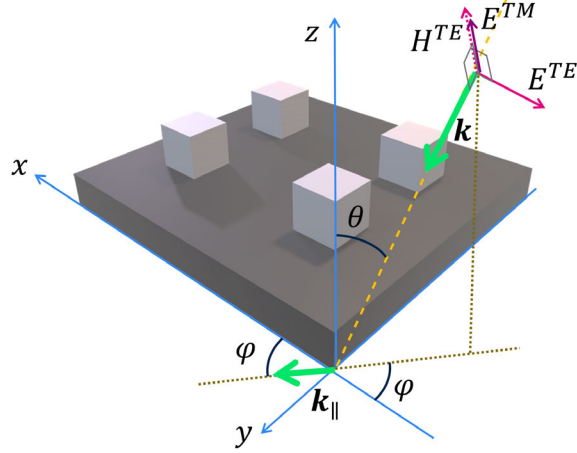
Figure 1: TE/TM geometric conventions for angles θ and φ for structures with square patterns, implying that the limit case $\theta = \varphi = 0°$ has Cartesian components E_y and H_x.

100 nm (a metamaterial), embedded between two thin Si layers ($t_h = 50$ nm forming essentially the h-FP mirrors as t_h is about $\lambda/4n_{Si}$) and spaced by silica (SiO$_2$, n$_{SiO_2} = 1.456$, $t_c = 150$ nm). In Fig.2(c,e), the RWG period is $d = 300$ nm, while in Fig.2(d,f), the h-FP period is $d = 250$ nm.

These structures deliberately comprise few layers and a simple grating pattern (a square "atom"), this latter being easily controlled in a CMOS process on a fairly large range of its filling factor f (fractional area in unit cell). The parameter f is the only geometrical feature that we modify in this paper to tune the filters' resonant wavelength, but period and layers thicknesses are as many handles to tune in further steps. A single period is preferred here to minimize efforts, but we advise to consider varying this parameter in future development, with the only provision that the period remains slightly sub-wavelength.

Note that this kind of structure can be assimilated to the so-called high-contrast-grating (HCG), studied in various respects, e.g., in [30, 31]. The opportunities offered by high-contrast structures are actually not limited to the membrane nature of "standard" HCG. The properties of such structures mostly stem from the way Bloch modes, launched vertically in the lamellar, high index contrast part of the structure, deal with the strong changes at the horizontal boundaries, promoting a very high reflection of targeted modes. A striking example are the "zero-contrast gratings" promoted by R.
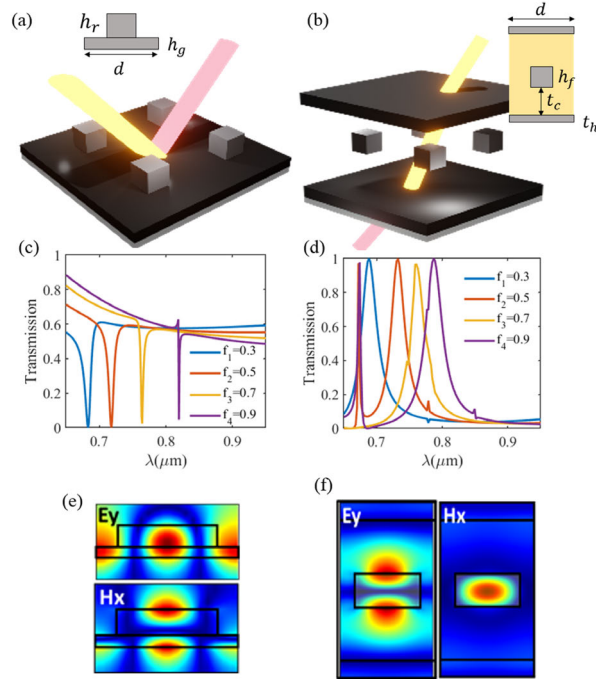
Figure 2: (a) Schematic representation of the RWG structure. As shown on top, h_r and h_g are the thicknesses of the 2D grating and the waveguide layer, d is the period. (b) Schematic representation of the h-FP cavity of period d, t_h is the thickness of the mirrors, h_f that of the 2D grating, and t_c that of the cavity. (c-d) The transmission spectra of the RWG and h-FP respectively for chosen filling factors f =0.3–0.9. (e-f) Electric E_y and magnetic H_x field distribution for RWG and FP filters respectively (z is the vertical direction and the cuts are in the xz plane).

Magnusson and co-workers[32, 33], that have formally the same shape as our RWG (uniform layer + square ridges of the very same high-index material, say silicon), but a substantially different aspect ratio, so as to exploit the Bloch modes interference properties. They perform much as our h-FP, with neat and narrow transmission peaks at normal incidence inside a large reflection band, but we found that they have large sensitivity to absorption loss and angle of incidence, so that an in-depth investigation would be needed to adapt them to the CMOS requirements considered in this paper.

The numerical method used in this work is the classical Fourier Modal Method (FMM) (also known as Rigorous Coupled Wave Analysis, RCWA)[34], implemented in a Matlab© homemade package (SimPhotonics). The number of plane-wave harmonics (typically a few tens in a given reciprocal space

direction) is adapted to the convergence needs. A first target of this study is the comparison of spectral responses of both structures when illuminated by a linearly polarized wave. Thus, in the following cases, a TE polarized plane wave irradiates structures at $\theta = 0°$ and $\phi = 0°$. A first criterion is to attain a fair degree and quality of tunability in the basic normal incidence case, this is what is developed in this section.

For the RWG, a narrow transmission dip (hence a reflection peak) is generated, Fig.2(c). This is due to the grating that couples the incident wave to a structure's leaky waveguide mode ($k = n_{\text{eff}} 2\pi/\lambda$) [35] with n_{eff} the effective index. Upon increasing f in the indicated domain ($0.3 \leq f \leq 0.9$), chosen in a feasible range process-wise, it is clearly seen that the reflection peak is red-shifted by $\Delta\lambda \sim 150\,\text{nm}$. This is due to the increase of n_{eff} via the increased grating average index. It is worth noting that the dip width decreases for large f (which can skew the spectral performance because it leaves more out-of-band photons and their noise masking the useful signal, and because of an increased angular sensitivity, notably if narrow lines are present in the spectra).

On the other hand, the h-FP filter (also made of solely a-Si and SiO_2) produces transmission peaks up to 100%, on account of well-known multiple interferences and energy storage inside the mirrors [5]. This peak varies in a similar red-shifted way as the RWG filter does with f, Fig.2(d), the basic reason being the sole average index (in other words, an effective index for a vertically propagating mode, now). While the RWG dip was narrowed for large filling factors f, the transmission peak in the h-FP filter retains its shape, its width, and its high transmission efficiency.

A comment is of order here about the finest features that arise in the spectral response of those periodic structures, Fig.2(c,d): they are related to low-loss guided modes. The existence of such modes is possible because we chose a loss-free model of a-Si. With minute material losses, these fine features are smeared out. In particular, for RWG structures with actual a-Si refractive indices (i.e. complex indices, with possibly a non-zero imaginary part), the incident signal in the visible range is mostly absorbed, and so resonances in this domain are attenuated or even non-existent, as seen experimentally in [36]. A common issue with a-Si is the deposition-method-dependent material dispersion, which is quite large. However, given the heuristic scope of this work, the simplest way to be general is to present data from loss-less and dispersion-less a-Si. For most cases that we are aware of, the principle and design guidance that we shall extract from this study shall fully hold. In the

last section, we nevertheless document the case of realistic dispersive and absorptive amorphous silicon, and find modest changes.

It is worth noting that the spectral response is polarization-independent due to the symmetric square lattice of the filters studied. In order to visualize the resonant modes in each kind of filter and grasp which features are critical, the electric and magnetic field distributions are calculated for TE polarization and at normal incidence ($\theta = 0°$, wave incident along z). The geometrical parameters of the RWG and the h-FP filters are chosen as mentioned before, with $f = 0.5$. For the RWG case, the resonance is found at $\lambda_{RWG} = 718\,$nm. Fig.2(e) shows respectively the y-component of the E field, and the x-component of the H field in the xz-plane, which both obey the expected normalized pattern for a (resonant) guided mode with wavevector k along x. For the h-FP case shown in Fig.2(f), still with $f = 0.5$, the resonance is at $\lambda_{FP} = 717\,$nm, the electric field pattern is concentrated on the top and bottom faces of the silicon atom, which points to the 2nd order FP mode with two vertical antinodes, while the magnetic field is concentrated inside the silicon atom. The E field is weak at both mirrors due to the overall π phase reflection of the thin a-Si high index slabs.

In terms of tunability, these resonant modes can be shifted as well by varying the period which will in turn displace the guided mode, as illustrated in Fig.3, which shows the effect of a change of the period d of the RWG and h-FP filters at constant filling factor $f = 0.5$. It has an effect similar to the change in filling factor. For the RWG, we see that this strategy circumvents the narrowing of the dip width seen in Fig.2(c). This could mitigate the drawbacks that we have seen in RWGs, but on the other hand it tends to imposes one strategy for the RWG (change of period) while the h-FP is more compatible with both.

At this point, because of its transmission characteristics, the h-FP approach seems to be more appropriate than the RWG approach for a spectrometer's job (i.e., well-shaped similar channels gently covering the IR range) even if the variable transmission dip shape of RWG based filters could be mitigated by varying the period too, leading to a more regular dip shape as seen in Fig.3. But in a system's perspective, those aspects of RWG at odds with a basic spectrometer picture could also be mitigated by signal processing taking into account its special response, an issue we address in Sec.4.
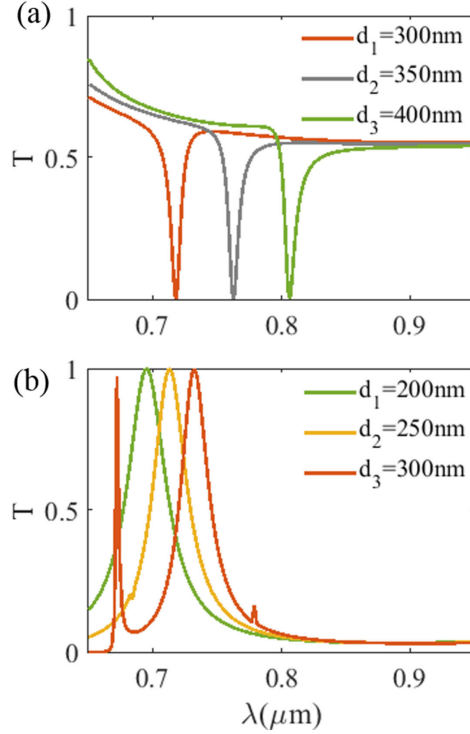
7

Figure 3: (a) Transmission spectra for RWG filters for different periods ($d = 300, 350, 400\,\text{nm}$), the same geometrical parameters are used $h_g = 25\,\text{nm}$, $h_r = 50\,\text{nm}$, and $f = 0.5$. (b) Transmission spectra for h-FP filters for different periods ($d = 200, 250, 300\,\text{nm}$), and with the same parameters as mentioned before, $t_c = 150\,\text{nm}$, $t_h = 50\,\text{nm}$, $h_c = 100\,\text{nm}$. This figure shows that tuning the resonant wavelength can be also done by adjusting the period of both structures (i.e. increasing the period red-shifts the resonance).

3. Polarization and angular tolerance

A second criterion for investigating the performance of the filters is to assess the angular tolerance of RWG vs h-FP under oblique incidence in both TE and TM polarizations. Fig.4(a–c) shows the transmission map of RWG structures (i.e. maps of $T(k_\parallel, \omega)$ with $k_\parallel = \sin\theta(2\pi/\lambda)$, where θ is the zenithal angle, that we nickname dispersion maps (given their salient features) in TE polarization for azimuthal angle $\phi = 0°$, $22.5°$, and $45°$ respectively. For Fig.4(a), at $\phi = 0°$, it appears that the RWG features are very sensitive to θ or $k_\parallel$, indeed the predicted behavior for a canonical grating waveguide ($k_\parallel + 2\pi/d = n_{\text{eff}}[2\pi/\lambda]$ at constant n_{eff}). In Fig.5(a,b), we remind the constant-frequency curves of basic guided modes (solid lines) and folded

8

(dotted lines) guided modes in the empty-lattice limit, in the k_x, k_y horizontal plane. At the exact second Bragg order, four arcs of circles intersect exactly at the Γ point ($k_x = k_y = 0$, normal incidence), at some frequency ω_1, as shown. For the case $\phi = 0°$, hence along k_x, the two modes associated to reciprocal wavevectors $\pm G_0 \mathbf{x}$ cause a strong dispersion branch, as appears by tracking colored dots that intersect the various circles in Fig.5(b,c), while the modes associated to reciprocal wavevectors $\pm G_0 \mathbf{y}$ give rise to a low-dispersion branch (it would be parabolic in the empty lattice limit, the situation is known as *conical* dispersion). As for the $\varphi = \pm 45°$ directions, the intersections (cyan and violet dots) of the ω_2 and ω_3 circles in Fig.5(b) indicate an intermediate dispersion, doubly degenerate in the empty lattice limit, as shown on on Fig.5(d). This explains the main large-scale features of the actual dispersion diagrams, with the two relevant cases of Fig.4 shown in Fig.5(e,f). Practically, in Fig.4(a) The resonant wavelength dip, salient at $0°$, is shifted from $(d/\lambda) = 0.415$ to 0.465 at the $20°$ red line, associated to $k = n_{\text{inc}} \sin 20° \omega/c$ (n_{inc} being the incident medium index), as a guided mode of larger wavevector is coupled. A companion mode with a smaller wavevector, in the opposite direction, appears at lower frequencies, but the specific structure of the guided modes near $k = 0$ cause a strong imbalance in that area. As for the third mode, less dispersive, it follows from Fig.5 that it results from a coupling to a pair of "conical" guided mode, propagating sideways. In the case of $\phi = 22.5°$, the pair splits while the upper and lower modes are less dispersive. Eventually, at $45°$, degeneracy of the four excited guided modes result in almost a single mode of intermediate dispersion.

Comparatively, the hybrid FP behaviour of Fig.4(d–f) is much less affected by azimuthal angle, as it does not rest on a coupling to another mode but pertains to the FP mode itself. A standard FP with a cavity of index n_{FP} would just have a dispersion dictated by a simple resonance condition such as $k_z = n_{\text{FP}} k_0 \cos(\theta)$ ($k_0 = 2\pi/\lambda$), hence $1/\lambda \propto 1/\cos(\theta) \simeq 1 + \theta^2/2$. Such a parabolic behaviour appears around $0°$ in case (d). But we checked that, much as in our previous 1D investigation [29], mode coupling effects due to the periodicity cause a $\sim$ twice lower dispersion than this naive prediction. The trend of flattening this usual FP dispersion is even more clear in (e-f), at $22.5°$ and $45°$. It is here a confirmation that the trends for such an hybrid FP to display limited angular dispersion for proper design are about equally valid in a 2D case and a square lattice as they were in 1D. There are a few thin "scars" superimposed on the main transmission peak, due to the coupling to guided modes carried by the FP edge slabs, among others, but they
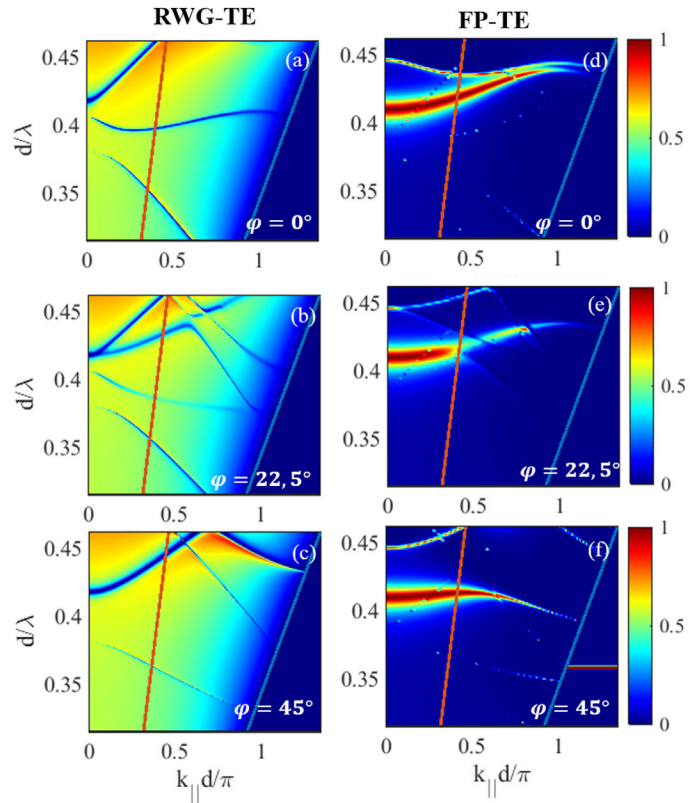
Figure 4: (a–c) TE transmission dispersion map for RWG filters for $\phi = 0°$, 22.5°, and 45° respectively. (d–f) TE transmission dispersion map for FP filters for $\phi = 0°$, 22.5°, and 45° respectively. The red line represents the light line at 20° in SiO_2, the blue line is the silica light line (i.e. waves at 90°).

negligibly degrade the main spectral peak.

It is likely that such extra features could be mitigated or even completely avoided by using shorter periods d that prevent coupling, operating deeper in the subwavelength regime and well below the light-line in a dispersion diagram. This would however entail larger aspect ratio (height/side) for the square shapes or square holes, adding to the burden of CMOS fabrication. Furthermore, as will be seen below, the targeted tasks such as spectral retrieval shall involve processing from a series of filters. In such conditions, an easier fabrication task with the proposed larger period d, followed by post-acquisition treatment that can be refined in an application-optimized manner and on much quicker time scales than CMOS fabrication runs seems a better choice at hand.
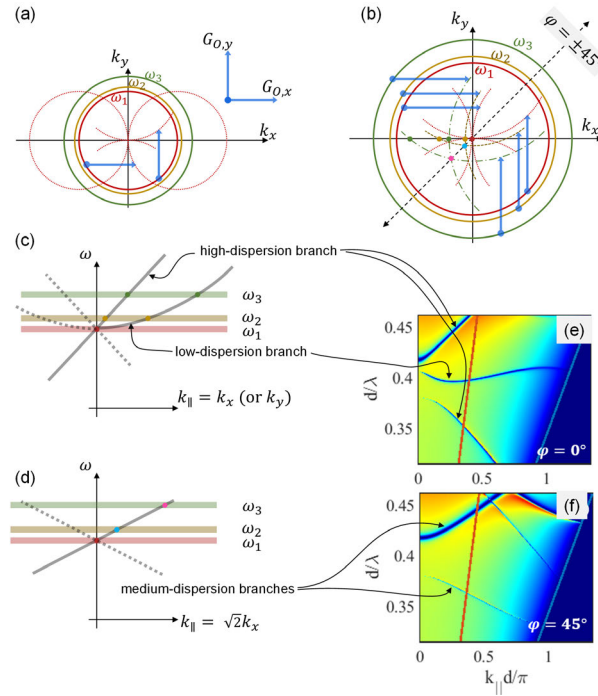

Figure 5: Angular dependence of RWG modes with square lattice: (a) circles of constant frequency for three frequencies $\omega_{1,2,3}$ (solid lines) and the replica of those at ω_1 due to the reciprocal vectors $\pm G_0 \mathbf{e}_x$ and $\pm G_0 \mathbf{e}_x$; (b) Zoom with some replica of circles at ω_2 and ω_3 added, and the $\pm 45°$ directions indicated; (c) Dispersion in the case of $\mathbf{k}_\parallel$ along the x axis, tracking the colored dots helps grasping the different origins of the low-dispersion and the high dispersion branches; (d) dispersion for $\mathbf{k}_\parallel$ along the $\pm 45°$ directions; (e,f) TE diagrams of above figure for the two directions.

11

Remarkably, for the TM case shown in Fig.6(a–c), we have a very different behaviour for the RWG. At 0° in particular, the resonant dip remains quite unaffected until $\theta \geq 20°$. This is due to the marked dominance of the "conical" modes discussed above, the coupling to the forward and backward modes being totally inhibited in this polarisation. The 45° situation is looking very much like a canonical bandgap, and the 22.5° is intermediate. Hence, even in a single polarisation, flattening the dispersion of a RWG only occurs as the exception, and cannot easily be the rule (it demands guided modes with an extended bandgap-type dispersion, as studied in Fehrembach works for small angles for instance [37, 38], but not commonly extended to the range we probe here, to our knowledge).

For the h-FP case shown in Fig.6(d–f), we see that the transmission peak remains quite flat till 20°, featuring a downward high-order bending at normal incidence. A standard upward bending is restored in (c) (45° case), albeit with a weaker curvature. An upper mode negative dispersion "scar" complexifies the behavior at angles just beyond 20°. It is not negligible, but quite weak yet. Here, the h-FP clearly features better in terms of angular tolerance. A single quantitative criterion does not render the exact impact on the system, though. Hence our attempts in the sections below to exploit these data at an upper level, that of an array of similar ALS sensors used for a desirable and canonical enough functionality: a spectral retrieval of a simple spectrum spanning typically 10 individual sensors (photodiodes), obtained by a "lithographic tuning" of the atom size only. Of course, a more thorough investigation can be set up, varying the period or other parameters as well, but we want to stay concise, and articulate more thoughtfully the relationship between a set of filter characteristics and a system-level figure-of-merit. We will do this on two grounds: exploiting the filters at normal incidence for spectral retrieval in section 4, and , in section 5, exploiting the filter across all their angular range for a similar task, but in a case where the spectral "noise" of the retrieved data is a "landscape noise" caused by a specific angular distribution of the scene, that will be described later.
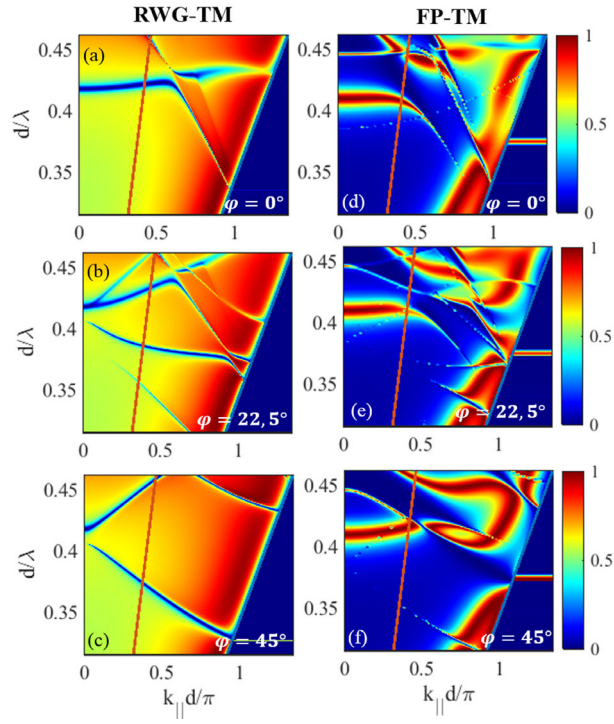
Figure 6: (a–c) TM transmission dispersion map for RWG filters for $\phi = 0°$, $22.5°$, and $45°$ respectively. (d–f) TM transmission dispersion map for FP filters for $\phi = 0°$, $22.5°$, and $45°$ respectively. The red line represents the light line at $20°$ in SiO_2, the blue line is the silica light line (i.e. waves at $90°$).

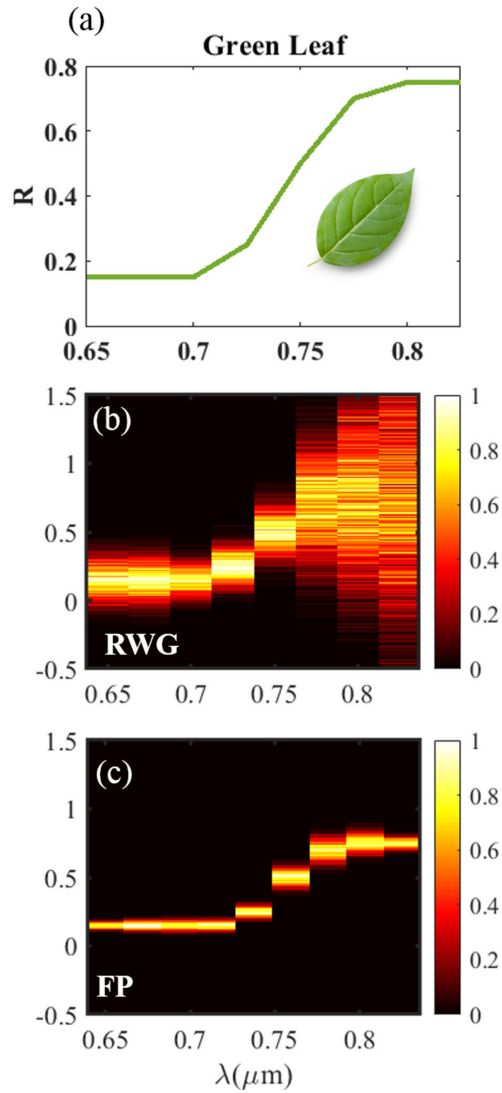Figure 7: (a) The reflection spectrum of a green leaf discretized at 8 wavelengths from $0.65\,\mu$m to $0.85\,\mu$m, with its characteristic rising edge. (b-c) Retrieved leaf spectrum from a RWG and FP filters respectively with their statistical spread, obtained by applying the inverses of the matrices M of Fig.8 to signals with added noise. The colormap indicates normalized abundances of each values, from a simulation over 1200 draws with added random noise.

4. Signal to noise ratio (SNR) related to the number of received photons

A reasonable "ALS target" for our purpose is to retrieve a coarse spectrum from a set of $N \approx 10$ ALS sensors with stepped filling factors $f_{j=1...N}$ interpolated from the three f values of Fig.2 (or slightly extrapolated to lower f values). Without noise, it boils down to an inversion problem with N degrees of freedom. Then, it suffices that the $N \times N$ matrix M relating N "spectral bins" to N ALS sensors has an inverse M^{-1}. In the presence of noise, the conditioning of M dictates how valuable the inversion is. Without the noise issue, matrices M for RWG and for h-FP should work equally well, with provisions for the vanishing dip width at larger f (the dip becoming much smaller than the spectral bin targeted). In the presence of
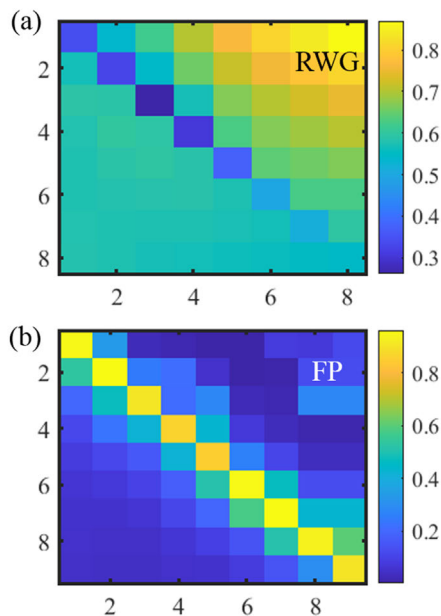

Figure 8: Filter matrices M representing the spectral response of each ALS pixel (lines) in each spectral channel (columns). (a) The RWG filter matrix for the studied case consisting of 8 filters between 650 and 825 nm. The diagonal blue squares track the useful filter dip ; (b) The h-FP filter matrix consisting of 9 filters between 650 and 825 nm, the diagonal yellow squares track the resonant transmission of each filter.

noise however (scaling, say, as photocurrent$^{1/2}$, a reasonable choice for a simple estimate of noise impact), it shall appear that the h-FP is more ad-

vantageous. To substantiate this discussion, we present the retrieval of the elementary leaf-type spectrum Fig.7(a), by RWG and h-FP filters Fig.7(b,c) respectively, with shades for the noise-induced scatter in the result (the colors map the histogram of occurrences). The corresponding matrices M are given in Fig.8(a,b). This type of spectrum with a strong infrared component is also known for perturbing cameras with ordinary Bayer filters, by enhancing the contribution of the various RGB channels that all have some tails in this spectral domain. Here, our spirit is more that of considering that ALS sensors could also become efficient systems for agricultural surveys for instance, whereby a drone or a harvesting engine must assess the quality of the crop through signals from the leaves, be it cereals or fruits, on trees or on the ground. Furthermore, for simplicity here, the spectrum (actually continuous) is discretely sampled only at the N values of interest, no spectral integration across bins is performed.

Here, we assume an incoming SNR (Signal-to-Noise Ratio) of 10 at the right tail of the spectrum, where photons are the most abundant. This modest SNR not only helps visualization, it also corresponds to the need of a quick inspection, much as the ALS used for assisting the color balance must deliver a predictive data prior to the first acquisition (with typical 20–100 ms integration times). Coming back to the photonic analysis of the issue (thus based on the inversion of matrix M of Fig.8(a) for the RWG filter), it is clear that even with the large photon "spectral intake" of the RWG pixel ($\geq 80\%$ of impinging light), i.e. a larger signal in each pixel, the retrieved leaf signal is blurred with an average noise $\sigma_{RWG} = 0.18$. This is a typical signature of non optimal conditioning, meaning in practice that signals are retrieved mostly thanks to subtraction among the individual pixel raw results. The larger spread in the last channels ($\lambda > 0.8\,\mu$m) is the most salient victim of this process, as the narrowing width of the RWG feature means that the subtraction concerns very close ideal signals. Such operations diminish the signal but not the noise, which still contributes in the same additive way for addition or subtraction.

Conversely, for the h-FP pixel, even though most of the impinging light is rejected ($\geq 80\%$), which is less favourable for a single-pixel SNR, it is much more successful in retrieving the leaf signal with an average noise $\sigma_{FP} = 0.05 \ll \sigma_{RWG}$. Here, the matrix M, Fig.8(b), is closer to a diagonal one and thus requires minimal subtractions to retrieve a spectrum.

This ability to better tolerate the noise in coarse spectral retrieval is positively factored when considering its better oblique incidence behavior.
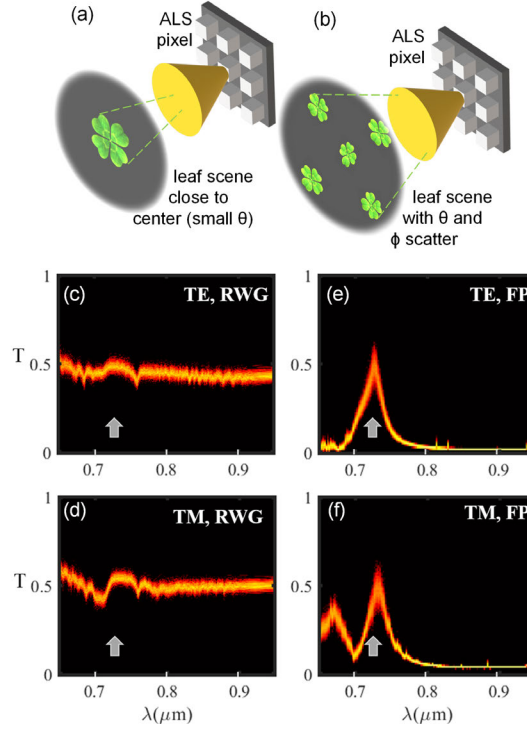
5. Landscape noise

Figure 9: Response of a selected ALS pixel with $f = 0.5$, thus centered at $0.725\,\mu\text{m}$, with its spread caused by the "landscape noise" issue of variable angular distribution for a given spectrum coming from objects on a darker background, pictured in the top schemes (a,b) and explained in Fig.10. The same colormap of the underlying histogram as in Fig.7 is used: (c-d) represent the average signal collected from the RWG filter for an open diaphragm (i.e. for θ span from 0° to 30° and for ϕ from 0° to 45°) for TE and TM polarization respectively. (e-f) represent the average signal collected from the h-FP filter for an open diaphragm (i.e. for θ span from 0° to 30° and for ϕ from 0° to 45°) for TE and TM polarization respectively.

In this section, we study the role of the angle tolerance in terms of inducing a kind of noise that we term "landscape noise". A well-known issue in any array is the spatial noise between adjacent pixels. In some technologies (e.g. Mercury-Cadmium Telluride in the mid-infrared), an insufficient fabrication homogeneity can be the main factor in performance degradation (the Noise Equivalent Temperature Difference NETD in this case).
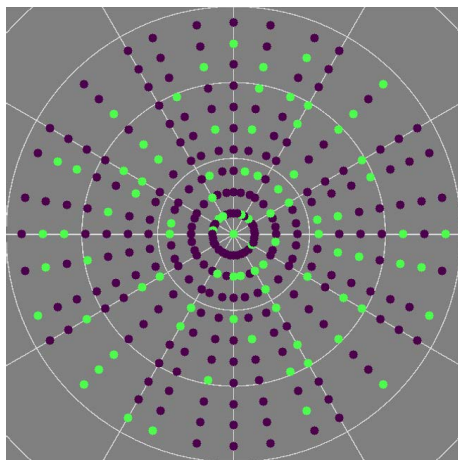
Figure 10: Schematic representation of the landscape spectral scene, with bright as green and dark as purple dots, which represents the light received by the filter at different solid angles (i.e. zenith and azimuth) from a specific scene. The choice of the bright and the dark is done using a random function with a specified ratio of the bright to the dark spots.

Here, we believe that a similar idea is relevant, but not in the real space of adjacent pixels (these pixels anyway differ in an ALS array) but in the dual space of scene directions (zenith and azimuth). If all directions of a scene emit (or scatter) the very same spectrum (that of a given leaf, say), but some parts of the solid angle captured are simply dark, the situation naturally causes a variable distribution of angles depending on the pattern of dark and "white" elements of the scene. Again, think of tens of plant leaves on a dark background, with leaves individual dimensions covering only a tiny bit of the captured solid angle, see the schemes Fig.9(a-b). Realistic numbers would be about 0.25% of the captured solid angle on average if, say, there are 100 leaves in a scene and they occupy 25% of the total solid angle. Figure 10 gives an example of such a "landscaped" spectral scene. Here, for the practical purpose of solid angle integration, it is presented as a kind of "dart game target", with bright (light green) and dark (purple) areas randomly assigned on a grid defined by a small set of polar angles θ (zenith) and of azimuth angles ϕ. We chose a grid that matches a reasonable set of angular (azimuth+zenith) simulations, with eleven θ values uniformly distributed (0° to 30°...), and $\phi(°) \in \{0, 10, 22.5, 30, 45, 60, 67.5, 80\}$ and their four rotated equivalent azimuths that logically cover the 360 degrees span of the solid angle explored with 32 azimuths. We take into account the
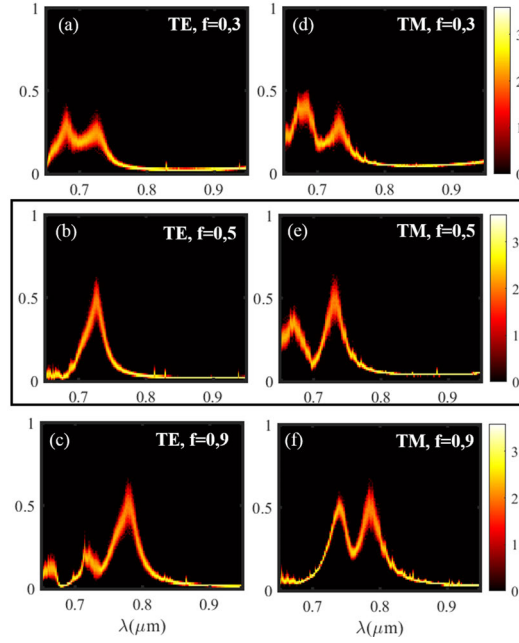
18

Figure 11: (a-b-c) Represent the TE average signal collected from the h-FP filter for an open diaphragm for different filling factors (f=0.3, 0.5, 0.9) respectively. (d-e-f) Represent the TM average signal collected from the h-FP filter for an open diaphragm for different filling factors (f=0.3, 0.5, 0.9) respectively. The appearance of extra peaks, especially in the TM case, comes from the appearance of extra resonances that play a role at large θ angles. The black rectangle situates the data already shown in Fig.9(e,f).

weight of the resulting specific solid angles in the integration. Those weights have a limited spread so that this computationally lighter choice accounts reasonably well for a "white landscape noise".
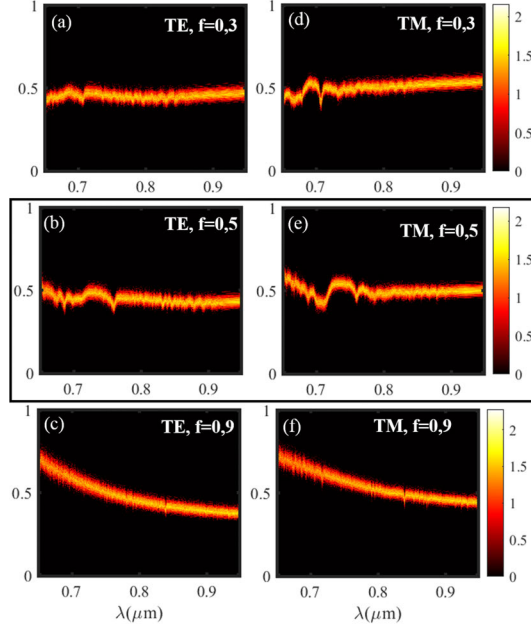
Figure 12: (a-b-c) Represent the TE average signal collected from the RWG filter for an open diaphragm for different filling factors (f=0.3, 0.5, 0.9) respectively. (d-e-f) Represent the TM average signal collected from the RWG filter for an open diaphragm for different filling factors (f=0.3, 0.5, 0.9) respectively. The black rectangle situates the data already shown in Fig.9(c,d). The appearance of extra peaks, especially in the TM case, comes from the appearance of extra resonances that play a role at large θ angles, and notably of the several branches that can be seen in Fig.6(b-c) when $\phi \neq 0°$.

A first step is to explore the kind of blurring of the spectral response caused by the averaging of a pattern that randomly occupies this solid angle grid with probability f_Ω =0.25. To this end, we simulated the four spectral histograms of Fig.9(c–f). In the absence of a specific metric for the "landscape noise", our goal is also heuristic. We thus show here only the signal captured by the fourth pixel that has selectivity at 725 nm (as a dip for RWG and as a peak for h-FP). We thus address the two kinds of filters and the two polarizations separately, in order to track the effects from the basic filter data of Fig.4 and 6.
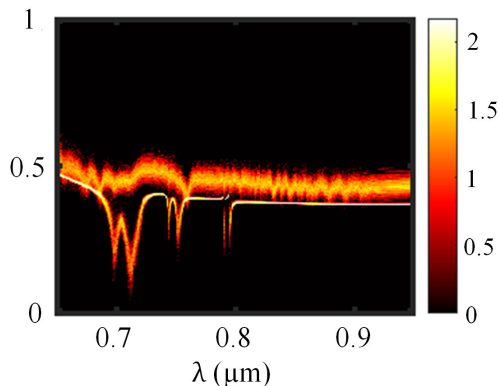
Figure 13: The landscape noise represented in two superimposed average spectra: the "thick" spectrum with full open diaphragm and the spectrum with the deeper and finer dips with a restricted 25% opened diaphragm. This unambiguously points out that the blurring of the RWG dip comes from the outermost angles of our angular θ distribution. The fact that the small angles do not incur much blurring suggests a possible window in these tighter limits for the possible use of RWG to provide spectral information.

We see that the RWG suffers most from the situation because, visually, the blurring is about a third the depth of the dip for both RWG polarizations whereas it represents about one-tenth of the peak height for the FP in TE polarization and a little less for the TM case. This means that upon inversion and spectrum retrieval by the same matrices as used in Figs.7,8, there would be a much larger spread. However, the issue of which further signal treatment can be done and which data is sought would modulate the conclusion to a large amount, so we prefer to pinpoint the issue at this stage and defer its treatment for later work. The advantage of the h-FP against this issue is nevertheless a sturdy fact in view of these simulated distributions.

We add in the end of this section some more histogram-rendering graphs that answer questions that might naturally arise about this spectral "landscape noise" concept that essentially deals with the interplay of spatial and spectral features.

21

To this end, figures Figs.11 to 13 illustrate the issue of landscape noise in relation with other parameters than those selected above. Fig.11 shows the kind of spread of the spectrum for the h-FP case and for filling factors of $f = 0.3$ (a,d) and $f = 0.9$ (c,f), reminding also in (b,e) in the black rectangle the $f = 0.5$ case chosen to illustrate Fig.9. It is seen that the relative spread of the histogram (from the orange center of histogram till the red color on its edge, say) is largely independent of f. For the RWG data, a similar exploration is reported in Fig.12, with the same extra filling factors $f = 0.3$ and 0.9 and the reminder $f = 0.5$ in the black rectangle. Here, the negative impact of a narrow dip for the angular tolerance can be easily seen: as the dip becomes very narrow at $f = 0.9$, the landscape-noise-induced blurring makes it nearly invisible. The case $f = 0.3$ retains nearly the same amount of dip visibility than $f = 0.5$. In Fig.13, we attempt to illustrate the limits that the landscape noise logically imposes: we see that by restricting the aperture to the 25% central solid angle, the depth of the spectral dips is substantially restored. In other words, and not surprisingly, it is the wide zenithal angle contributions that blur the response (even though there is no azimuthal symmetry with square gratings, so, in other words, the azimuthal comes second in terms of landscape noise). To summarize this point, the use of RWG is possible but with very substantial constraints on the aperture.

6. Dispersion and absorption of amorphous silicon

Finally, we address here the issue of material dispersion and absorption. We found in the above that it was sufficient and heuristic to use a single and purely real refractive index (no absorption) for amorphous silicon (while dispersion of silica is a minor issue anyway).
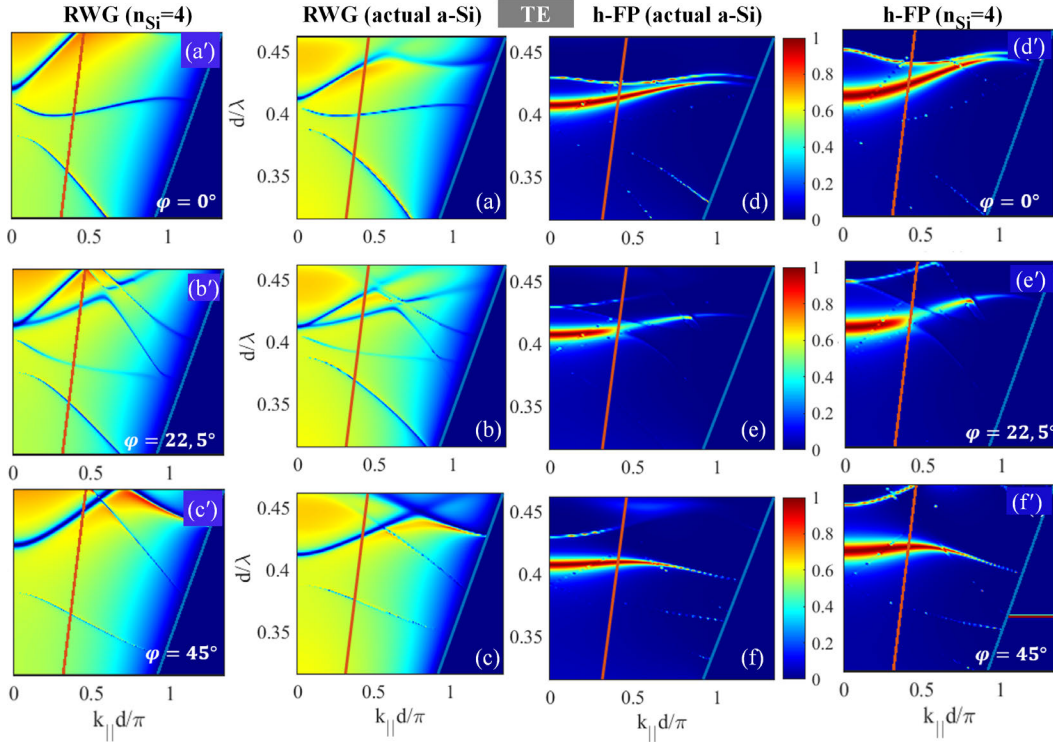

Figure 14: Comparison between TE response of both RWG and h-FP filters for a dispersive case (a–f), where the refractive index of a-Si is taken to be varying with the incident wavelength (dispersive case, Fig.16 below), with the six corresponding TE nondispersive responses (a'–f') shown above in Fig.4; (a–c) TE transmission map for RWG filters for $\phi = 0°$, 22.5°, and 45° respectively. (d–f) TE transmission map for h-FP filters for $\phi = 0°$, 22.5°, and 45° respectively. The red line represents the light line at 20° in SiO$_2$, the blue line is the silica light line (i.e. waves at 90°). Compared to Figs.4,6, the consideration of a dispersive index leads to some frequency distortions and shifts of the response. Also, some resonant frequencies vanished, probably due to the absorption of a-Si in concerned bandwidths.

23

This choice was motivated by the idea of making the study general and easy to explain and reproduce, focused on its photonic approach. However the impact of the actual dispersive refractive index of amorphous silicon must be assessed. Using the data of Fig.16 for amorphous silicon, which is a set that comes from actual fabrication facilities, we have investigated the various spectral responses in order to assess the amount of modification caused by the dispersion and the absorption. The angular-spectral TE map and TM map are reported in Figs.14 and 15 respectively, with illustrative angles $0°$, $22.5°$ and $45°$, compared in each figure to the six similar panels of Fig.4 and Fig.6 with the non dispersive value $n_{Si} = 4$: they are reminded in each figure in the rightmost and leftmost panels (a'–c') and (d'–f').
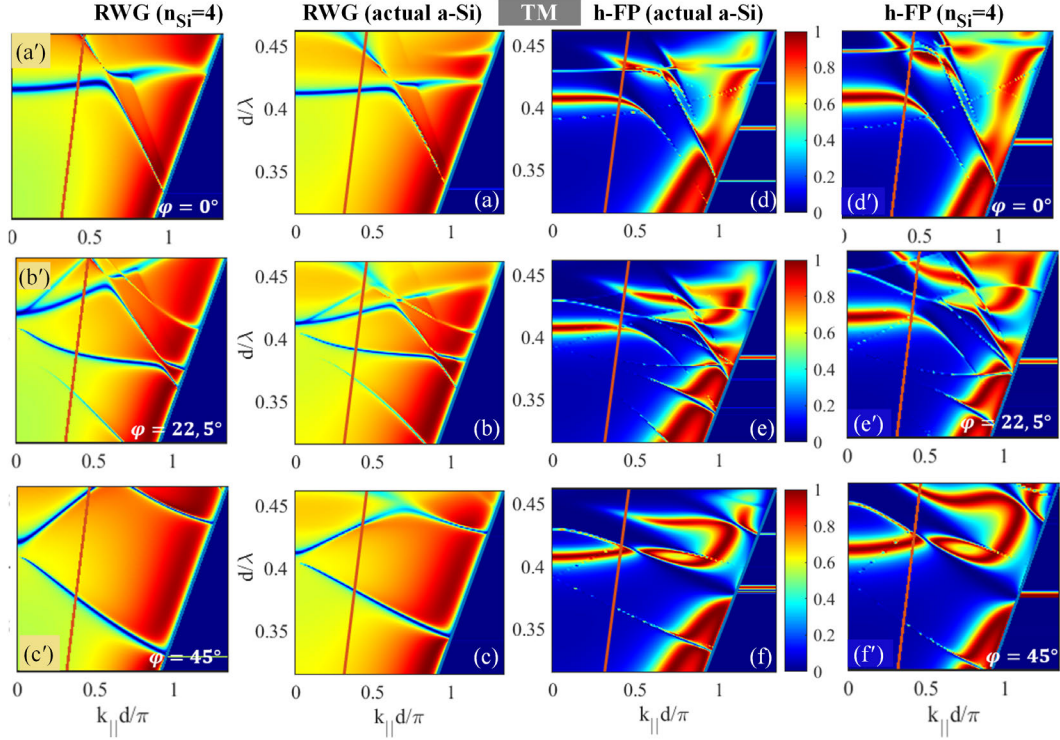
Figure 15: Comparison between TM response of both RWG and h-FP filters for a dispersive case (a–f), where the refractive index of a-Si is taken to be varying with the incident wavelength (dispersive case, Fig.16 below), with the six corresponding TM nondispersive responses (a'–f') shown above in Fig.6; (a–c) TM transmission map for RWG filters for $\phi = 0°$, 22.5°, and 45° respectively. (d–f) TM transmission map for h-FP filters for $\phi = 0°$, 22.5°, and 45° respectively. The red line represents the light line at 20° in SiO_2, the blue line is the silica light line (i.e. waves at 90°). Remarks similar to those of Fig.14 apply to the differences.
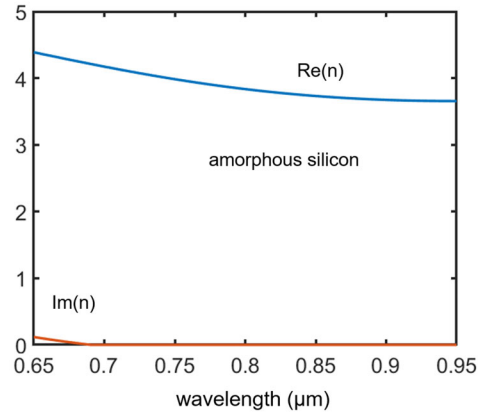
25

Figure 16: Real and Imaginary parts of the refractive index of the adopted amorphous silicon a-Si in the calculations of Fig.14 and 15.

The important point as regards dispersion is that the changes are limited. The most apparent is the vertical compression due to the large dispersion of the real index, and the other changes consist mostly of modest distortions and shifts in the lower frequency region. Hence, our photonic designs are not sensitive to this kind of typical dispersion. As for absorption, at the highest frequencies where amorphous silicon absorption sets in, a few sharp resonant features are smoother (top right of maps). Nevertheless the overall behaviour remains similar to the dispersionless case.

7. Conclusion

As a conclusion, in this study we provide a summary of the challenging aspects in CMOS sensors to realize near-infrared filtering structures compatible with CMOS technology, as a guidance for technology developers, thus with the capability of building a whole filtering matrix in a single lithographic step. The RWG, that works in rejection mode in the IR range, are a first choice due to their more basic fabrication with a mere silica cover. For h-FP see structures, additional steps on the cover side are needed, but the filters' tolerance vs incident angles is increased. Additionally, signal treatment may be easier and better with transmission filters (cf. Fig.7), all these advantages pointing toward the h-FP filter as an excellent trade-off between process, ease of use, and spectral response of these filters.

8. Acknowledgments

References

[1] K. D. Hakkel, M. Petruzzella, F. Ou, A. van Klinken, F. Pagliano, T. Liu, R. P. van Veldhoven, A. Fiore, Integrated near-infrared spectral sensing, Nature Communications 13 (1) (2022) 1–8.

[2] X. He, Y. Liu, K. Ganesan, A. Ahnood, P. Beckett, F. Eftekhari, D. Smith, M. H. Uddin, E. Skafidas, A. Nirmalathas, et al., A single sensor based multispectral imaging camera using a narrow spectral band color mosaic integrated on the monochrome CMOS image sensor, APL Photonics 5 (4) (2020) 046104.

[3] M. Kulkarni, V. Gruev, Integrated spectral-polarization imaging sensor with aluminum nanowire polarization filters, Opt. Express 20 (21) (2012) 22997–23012.

[4] H. Shen, X. Meng, L. Zhang, An integrated framework for the spatio–temporal–spectral fusion of remote sensing images, IEEE Transactions on Geoscience and Remote Sensing 54 (12) (2016) 7135–7148.

[5] B. Geelen, N. Tack, A. Lambrechts, A compact snapshot multispectral imager with a monolithically integrated per-pixel filter mosaic, in: Advanced fabrication technologies for micro/nano optics and photonics VII, Vol. 8974, International Society for Optics and Photonics, 2014, p. 89740L.

[6] S. Junger, N. Verwaal, W. Tschekalinskij, N. Weber, Near-infrared cut-off filters based on CMOS nanostructures for ambient light sensors and image sensors, in: Photonic and Phononic Properties of Engineered Nanostructures IV, Vol. 8994, International Society for Optics and Photonics, 2014, p. 89941K.

[7] I. Hussain, A. J. Bora, D. Sarma, K. U. Ahamad, P. Nath, Design of a smartphone platform compact optical system operational both in visible and near infrared spectral regime, IEEE Sensors Journal 18 (12) (2018) 4933–4939.

[8] S. Dutta, Point of care sensing and biosensing using ambient light sensor of smartphone: Critical review, TrAC Trends in Analytical Chemistry 110 (2019) 393–400.

[9] K. G. Rew, Plasmonic filters for ambient and near infrared sensing on CMOS, Ph.D. thesis, University of Glasgow (2017).

[10] F. V. Topalis, L. T. Doulos, Ambient light sensor integration, Handbook of Advanced Lighting Technology; Springer: Cham, Switzerland (2017) 607–634.

[11] C. Ding, Z. Ma, Multi-camera color correction via hybrid histogram matching, IEEE Transactions on Circuits and Systems for Video Technology 31 (9) (2020) 3327–3337.

[12] M. Bryson, M. Johnson-Roberson, O. Pizarro, S. B. Williams, True color correction of autonomous underwater vehicle imagery, Journal of Field Robotics 33 (6) (2016) 853–874.

[13] S. Chen, A. Pande, P. Mohapatra, Sensor-assisted facial recognition: an enhanced biometric authentication system for smartphones, in: Proceedings of the 12th annual international conference on Mobile systems, applications, and services, 2014, pp. 109–122.

[14] P.-G. Dittrich, M. Bichra, C. Pfützenreuter, M. Rosenberger, G. Notni, Measurement principle and arrangement for the determination of spectral channel-specific angle dependencies for multispectral resolving filter-on-chip CMOS cameras, in: Photonics and Education in Measurement Science 2019, Vol. 11144, International Society for Optics and Photonics, 2019, p. 111440S.

[15] M. Jayapala, A. Lambrechts, N. Tack, B. Geelen, B. Masschelein, P. Soussan, Monolithic integration of flexible spectral filters with CMOS image sensors at wafer level for low cost hyperspectral imaging, in: International Image Sensor Workshop, 2013, p. 1.

[16] S. Livens, B. Delauré, A. Lambrechts, N. Tack, Hyperspectral imager development using direct deposition of interference filters, in: The Small Satellites Systems and Services Symposium, 2014, p. 1.

[17] J. J. Cadusch, J. Meng, B. J. Craig, V. R. Shrestha, K. B. Crozier, Visible to long-wave infrared chip-scale spectrometers based on photodetectors with tailored responsivities and multispectral filters, Nanophotonics 9 (10) (2020) 3197–3208.

[18] I. Kim, J. Yun, T. Badloe, H. Park, T. Seo, Y. Yang, J. Kim, Y. Chung, J. Rho, Structural color switching with a doped indium-gallium-zinc-oxide semiconductor, Photonics Research 8 (9) (2020) 1409–1415.

[19] P. Cheben, R. Halir, J. H. Schmid, H. A. Atwater, D. R. Smith, Sub-wavelength integrated photonics, Nature 560 (7720) (2018) 565–572.

[20] P. Dai, Y. Wang, Y. Hu, C. de Groot, O. Muskens, H. Duan, R. Huang, Accurate inverse design of Fabry–Perot-cavity-based color filters far beyond sRGB via a bidirectional artificial neural network, Photonics Research 9 (5) (2021) B236–B246.

[21] L. Bibbò, K. Khan, Q. Liu, M. Lin, Q. Wang, Z. Ouyang, Tunable narrowband antireflection optical filter with a metasurface, Photonics Research 5 (5) (2017) 500–506.

[22] J. Berzinš, S. Fasold, T. Pertsch, S. M. Bäumer, F. Setzpfandt, Submicrometer nanostructure-based RGB filters for CMOS image sensors, ACS Photonics 6 (4) (2019) 1018–1025.

[23] Y. Horie, S. Han, J.-Y. Lee, J. Kim, Y. Kim, A. Arbabi, C. Shin, L. Shi, E. Arbabi, S. M. Kamali, et al., Visible wavelength color filters using dielectric subwavelength gratings for backside-illuminated CMOS image sensor technologies, Nano Letters 17 (5) (2017) 3159–3164.

[24] Z. Xu, N. Li, Y. Dong, Y. H. Fu, T. Hu, Q. Zhong, Y. Zhou, D. Li, S. Zhu, N. Singh, Metasurface-based subtractive color filter fabricated on a 12-inch glass wafer using a CMOS platform, Photonics Research 9 (1) (2021) 13–20.

[25] A. McClung, S. Samudrala, M. Torfeh, M. Mansouree, A. Arbabi, Snapshot spectral imaging with parallel metasystems, Science advances 6 (38) (2020) eabc7646.

[26] C. Yang, L. Hong, W. Shen, Y. Zhang, X. Liu, H. Zhen, Design of reflective color filters with high angular tolerance by particle swarm optimization method, Opt. Express 21 (8) (2013) 9315–9323.

[27] B.-H. Cheong, O. Prudnikov, E. Cho, H.-S. Kim, J. Yu, Y.-S. Cho, H.-Y. Choi, S. T. Shin, High angular tolerant color filter using subwavelength grating, Appl. Phys. Lett. 94 (21) (2009) 213104.

[28] L. Masarotto, L. Frey, M. Charles, A. Roule, G. Rodriguez, R. Souil, C. Morales, V. Larrey, Transmission measurements of multilayer interference filters developed for a full integration on complementary metal oxide semiconductor chips, Thin Solid Films 631 (2017) 23–28.

[29] F. Omeis, M. Besbes, C. Sauvan, H. Benisty, Highly angular tolerant transmission filters for narrow-band image sensors, Optics and Photonics Journal 11 (6) (2021) 140–151.

[30] C. J. Chang-Hasnain, W. Yang, High-contrast gratings for integrated optoelectronics, Adv. Opt. Photon. 4 (3) (2012) 379–440.

[31] H. S. Nguyen, F. Dubois, T. Deschamps, S. Cueff, A. Pardon, J.-L. Leclercq, C. Seassal, X. Letartre, P. Viktorovitch, Symmetry breaking in photonic crystals: On-demand dispersion from flatband to dirac cones, Phys. Rev. Lett. 120 (2018) 066102.

[32] R. Magnusson, Wideband reflectors with zero-contrast gratings, Opt. Lett. 39 (15) (2014) 4337–4340.

[33] M. Niraula, J. W. Yoon, R. Magnusson, Single-layer optical bandpass filter technology, Opt. Lett. 40 (21) (2015) 5062–5065.

[34] L. Li, New formulation of the Fourier modal method for crossed surface-relief gratings, J. Opt. Soc. Am. A 14 (10) (1997) 2758–2767.

[35] S. S. Wang, R. Magnusson, Theory and applications of guided-mode resonance filters, Appl. Opt. 32 (14) (1993) 2606–2613.

[36] S. Villenave, S. Monfray, H. Benisty, Q. Abadie, S. Audran, S. Guillaumet, B. Vianne, D. Ristoiu, F. Leverd, E. Sungauer, P. Chevalier, Advanced optical filtering based on si nanodisk integration on 300 mm glass wafer, SSDM conference, 7-9 september 2021, online in Japan (2021) E2–03.

[37] A. Sentenac, A.-L. Fehrembach, Angular tolerant resonant grating filters under oblique incidence, J. Opt. Soc. Am. A 22 (3) (2005) 475–480.

[38] E. Popov, A.-L. Fehrembach, Y. Brûlé, G. Demésy, P. Boyer, Two-dimensional grating for narrow-band filtering with large angular tolerances, Opt. Express 24 (13) (2016) 14974–14985.